Full field modeling of dynamic recrystallization in a CPFEM context – Application to 304L steel

David Alejandro Ruiz Sarrazola, Ludovic Maire, Charbel Moussa, N. Bozzolo, Daniel Pino Muñoz, Marc Bernacki

Version of Record: https://www.sciencedirect.com/science/article/pii/S0927025620303839
Manuscript_607a88fa3aac2e7d7c87d51a6109ee2b

Full field modeling of Dynamic Recrystallization in a CPFEM context - Application to 304L steel

D. A. Ruiz Sarrazola[a,*], L. Maire[a], C. Moussa[a], N. Bozzolo[a], D. Pino Muñoz[a], M. Bernacki[a]

[a] *MINES ParisTech, PSL - Research University, CEMEF - Centre de mise en forme des matériaux, CNRS UMR 7635, CS 10207 rue Claude Daunesse, Sophia Antipolis Cedex 06904, France.*

Abstract

In this work the recently proposed full field approach to model dynamic recrystallization [1] is applied to model 304L steel. The framework couples a CPFEM (crystal plasticity finite element method) model with a LS-FE (level-set finite element method) for grain boundary migration and phenomenological laws. 304L steel samples are subjected to thermomechanical tests and their flow behaviour is characterized, additionally Electron Back Scattered Diffraction is used to study microstructure evolutions. Part of the experimental data is used to calibrate the model parameters and describe their evolution as a function of the thermomechanical conditions. The calibrated model is used to predict the microstructural evolution of 304L steel. The results are compared with other experimental measurements, and show that the model correctly predicts the flow behaviour and recrystallization fraction evolution. However the results also show that the use of classical phenomenological models limit the model capability to predict grain size evolution. Different approaches to improve the model grain size prediction are presented and compared, the results show significant improvements when compared with experimental data.

Keywords: Dynamic recrystallization, Crystal plasticity, Level-set, 304L steel, EBSD, FEM, Full field model

*Corresponding author
Email address: david-alejandro.ruiz_sarrazola@mines-paristech.fr (D. A. Ruiz Sarrazola)

1. Introduction

Accurately modeling and predicting the evolution of the microstructure of metals subjected to metal forming operations, is required to be able to control their microstructure evolution. Controlling microstructure evolutions allows to produce metals with superior mechanical properties for industrial applications.

Dynamic recrystallization is one of the main processes by which the microstructure of metals evolves when subjected to hot forming operations. It is a major field of interest for researchers and several numerical models have been proposed. The models presented in the literature include: phenomenological models, like JMAK type models [2, 3, 4]; mean field models [5, 6, 7, 8, 9]; full field probabilistic models, like the Monte-Carlo and some Cellular Automata models [10, 11, 12]; full field deterministic models, like the vertex model [13, 14], level-set [15, 16, 17, 18, 19] and phase-field models [20, 21].

A brief description of the different models and their limitations was already presented in the first part of this work [1], and detailed reviews can be found in the literature [22, 23]. Most recrystallization models are fundamentally growth models with limited detailed descriptions of the underlying physical phenomena involved [24]. In order to provide a better description of the underlying physics, a new full field approach for dynamic recrystallization that couples a CPFEM model with a LS-FE for GB migration was proposed.

The proposed approach is a significant improvement of the previously published work [19]. The use of CPFEM provides a more physical description of plastic deformation phenomena, and serves as a basis for a better descriptions of the recrystallization phenomena involved in discontinuous dynamic recrystallization (DDRX). The purpose of this article is to compare the results of the model described in [1] to experimental data. In this regard, the behaviour of 304L steel subjected to hot deformation is simulated and the model results are compared to experimental measurements.

In the first section the experimental methodology and experimental data processing are presented. In a second part, the model results are compared with the experimental measurements and the model limitations notably in terms of twin boundaries consideration, recrystallized grains identification and grain size prediction are discussed.

2. Experimental Methods

Hot-compression tests were performed on 304L steel samples to reproduce industrial forging processes. The tests were performed for different sets of conditions in terms of strain rate and temperature.

The thermomechanical path is defined by the following steps: (A) The sample is put in the pre-heated oven. (B) The sample is kept at high temperature for 30 minutes to homogenize its temperature. (C) The sample is compressed at constant strain rate up to a given stain level. (D) The sample is water-quenched with the minimal possible delay, (i.e. around 2 seconds) to stop post-dynamic microstructural evolutions.

The test were performed in a MTS Landmark 370-25 compression machine equipped with a 2000 W oven. The lower and upper tools are made of superalloy Udimet 720, with a silicon nitride (Si_3N_4) ceramic insert, and molybdenum disulphide (MoS_2) as a lubricant. Two sample geometries (shown in figure 1) were tested, cylindrical samples to asses stress-strain curves and investigate the microstructure at low strain levels, and double-cone samples to investigate the microstructure at high strain levels.

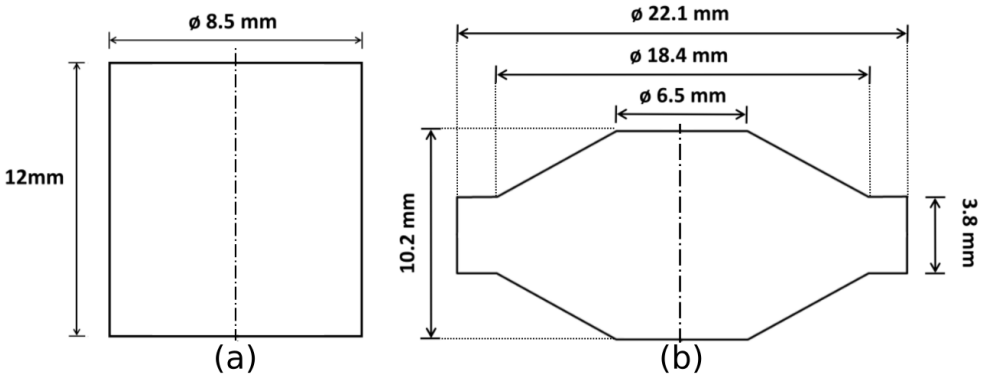

Figure 1: Sample geometries used in the thermomechanical test, cylindrical samples (a) and double-cone samples (b). Dash-Dot lines indicate revolution axis.

After the compression test, the samples were cut along the compression axis through the diameter, and polished in order to perform EBSD (Electron Back-Scatter Diffraction) measurements on specific points. On the cylindrical samples EBSD measurements were taken at the center of the longitudinal section, and on the double-cone samples the measurements were performed

at the center and at distance of $R/3$ from the center of the longitudinal section, with R the radius of the deformed sample.

The local strain and strain rate level at the measurement points (given in table 1) table were estimated from FEM simulations of the compression tests, performed using the software Forge®. The EBSD measurements were done using a Zeiss Supra 40 FEG SEM (Field Emission Gun Scanning Electron Microscope) equipped with a Bruker EBSD system. EBSD maps were acquired with a 0.47 μm step size, over an area of 250 μm by 330 μm, chosen to compromise between spatial resolution, test time and statistical representativity.

A - Test conditions for stress-strain curves (Cylindrical samples)						
	Nominal Strain rate $\dot{\epsilon}(1/s)$					
$T(K)$	0.008	0.01	0.04	0.05	0.08	0.1
1273	$0-0.4$	$0-0.7^*$	$0-0.4^*$	$0-0.7$	$0-0.7^*$	$0-0.7$
1323	$0-0.4^*$	$0-0.7^*$				
1373	$0-0.4$	$0-0.7$				

B - Test conditions for EBSD measurements						
	Cylindrical samples			Double-cone samples		
	Local Strain rate $\dot{\epsilon}(1/s)$			Local Strain rate $\dot{\epsilon}(1/s)$		
$T(K)$	0.014	0.07	0.14	0.014	0.07	0.14
1273	0.65	0.65^*	0.65	$1.00, 1.35$	$1.00, 1.35^*$	$1.00, 1.35$
1323	0.65^*			$1.00, 1.35^*$		
1373	0.65			$1.00, 1.35$		

Table 1: Conditions considered for the experimental test, strain rate, temperatures, strain range (stress-strain curves - Table A) and strain level (EBSD measurements - Table B). $(*)$ Indicates data sets used for the model validation.

The EBSD measurements were post-treated using the **MTEX** toolbox [25]. On the EBSD maps recrystallized grains were identified following the procedure described by Nicolay et al. [26]. Grains with size below 1.5 μm or with grain average misorientation GAM (Eq. 1), lower than 1 degree were considered as recrystallized.

$$GAM = \frac{\sum_{i=1}^{n} KAM_i}{n} \ , \tag{1}$$

with n the total number of pixels belonging to the grain and KAM_i the kernel average misorientation of each pixel i of the grain defined as:

$$KAM_i = \frac{\sum_{j=1}^{m} \theta_{ij}}{m} \ , \tag{2}$$

with m the total number of neighbor pixels of a pixel i and θ_{ij} the misorientation between the pixel i and its neighbor j. Consistently with the misorientation threshold applied for grain detection, values of misorientation θ_{ij} higher than 10° are not considered.

EBSD data were also used to calculate: the recrystallized area fraction X, defined by Eq. 3; the mean grain size (2D) $\bar{D}_{N2D}$, defined by Eq. 4 and the mean grain size weighted by surface $\bar{D}_S$, defined by Eq. 5.

$$X = \frac{\sum_{i=1}^{N_X} S_{Xi}}{S_T} \ , \tag{3}$$

with N_X the number of recrystallized grains, S_{Xi} the surface (2D) of each recrystallized grain, and S_T the total area of the EBSD map.

$$\bar{D}_{N2D} = \frac{\sum_{i=1}^{N} d_i}{N} \ , \tag{4}$$

with N the total number of grains, d_i the equivalent circle diameter (2D) of each grain defined as $d_i = 2 * \sqrt{S_i/\pi}$.

$$\bar{D}_S = \frac{\sum_{i=1}^{N} d_i S_i}{S_T} \ , \tag{5}$$

with S_i the surface (2D) of each grain. Considering that the numerical model to be tested is a 3D model, 3D data was required in order to calibrate and validate it. So, 2D grain size distributions by number fraction and surface fraction were calculated and transformed into equivalent 3D grain size distributions by number fraction using the **inverse Saltykov** method [27]. The 3D grain size distributions by number fraction were used to calculate the 3D grain size distributions by volume fraction.

The mean 3D grain size weighted by number fraction $\bar{D}_{N3D}$, defined by Eq. 6 and the mean 3D grain size weighted by volume fraction $\bar{D}_V$, defined by Eq. 7, were also computed from both 3D distribution.

$$\bar{D}_{N3D} = \frac{\sum_{i=1}^{N} d_{3Di}}{N} \ , \tag{6}$$

with d_{3Di} the equivalent sphere diameter (3D) of each grain, defined as $d_{3Di} = 2 * (0.75(1/\pi)V_i)^{1/3}$.

$$\bar{D}_V = \frac{\sum_{i=1}^{N} d_{3Di} V_i}{V_T} \ , \tag{7}$$

with V_i the volume (3D) of each grain, and V_T the total volume. For the initial state of the microstructure $\bar{D}_{N3D} = 33.23$ (μm) and $\bar{D}_V = 86.53$ (μm). The X and the $\bar{D}_V$ values were used for the comparisons with the model results.

3. Experimental Results

3.1. Thermomechanical tests

The stress-strain curves obtained from the thermomechanical tests, were smoothed using high order polynomial interpolation, to reduce the experimental noise (Figure 2). In general terms the curves show the expected behavior, with the stress increasing with increase in strain rate, and decreasing with the increase in temperature.

However, the used experimental set up does not allow to obtain accurate measurements at low strain levels. This makes difficult the identification of the macroscopic yield stress σ_0, so the values were taken from the literature [28].

3.2. EBSD Measurements

In order to process the EBSD measurements, grains were detected as groups of neighbouring points with less than 10° misorientation angle. Twin boundaries, identified by 60° rotation around the $\langle 1, 1, 1 \rangle$ axis with a 5° tolerance, were ignored in the grain detection procedure as they are not considered in the model. Figure 3 shows the EBSD map of the initial microstructure with and without twin boundaries, and the pole figures of the (001), (111) and (110) planes. The pole figures show that no preferred orientation is present in the initial microstructure.

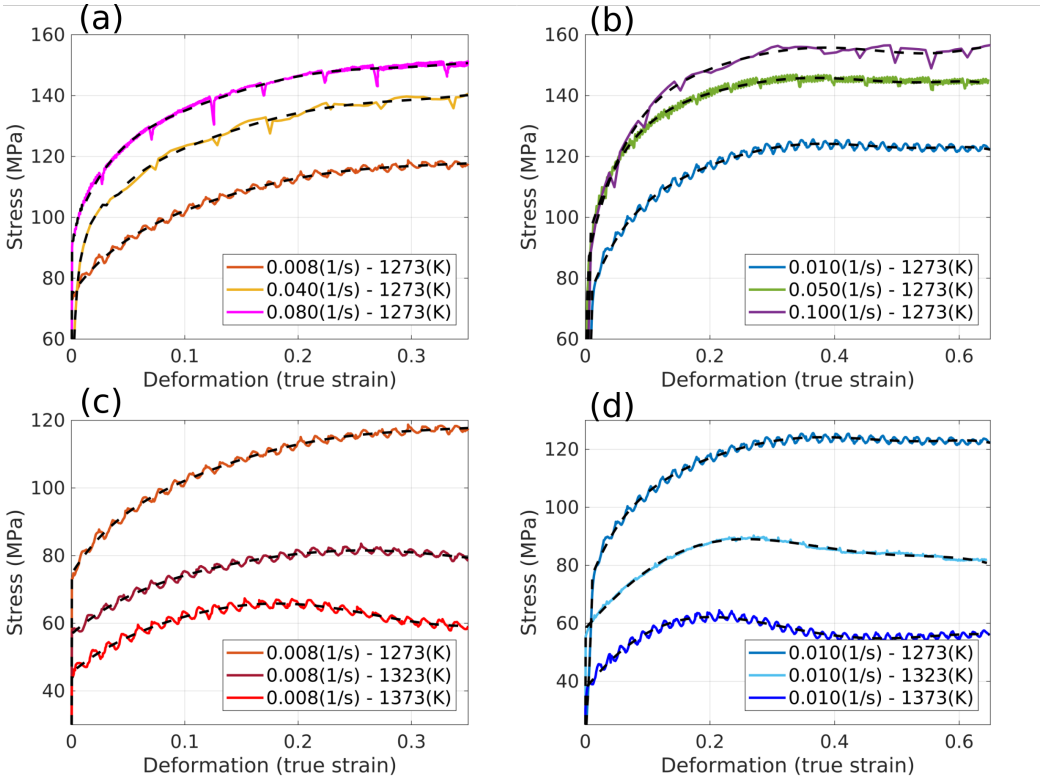

Figure 2: Measured (continuous lines) and interpolated (discontinuous lines) stress-strain curves for 304L steel cylindrical samples subjected to compression tests at high temperatures. Curves are grouped by temperature ((a) and (b)) and strain rate ((c) and (d)). Oscillations are artifacts due to periodic change in the tool velocity to follow imposed constant strain rate.

However, deformation causes that twin boundaries deviate from the 60° $\langle 1\ 1\ 1 \rangle$ ideal misorientation, so that some of them, or some parts of them, can get out of this tolerance. As a consequence, on highly deformed microstructures, it is not possible to correctly identify all the twin boundaries present in the microstructures. Figure 4 shows an EBSD map of a deformed sample with the twin boundaries plotted in red and grain boundaries excluding twins plotted in black. The EBSD maps show that twin boundaries are no longer identified as continuous lines and part of them is considered as a normal grain boundary, this can cause an artificial reduction in the measured grain size.

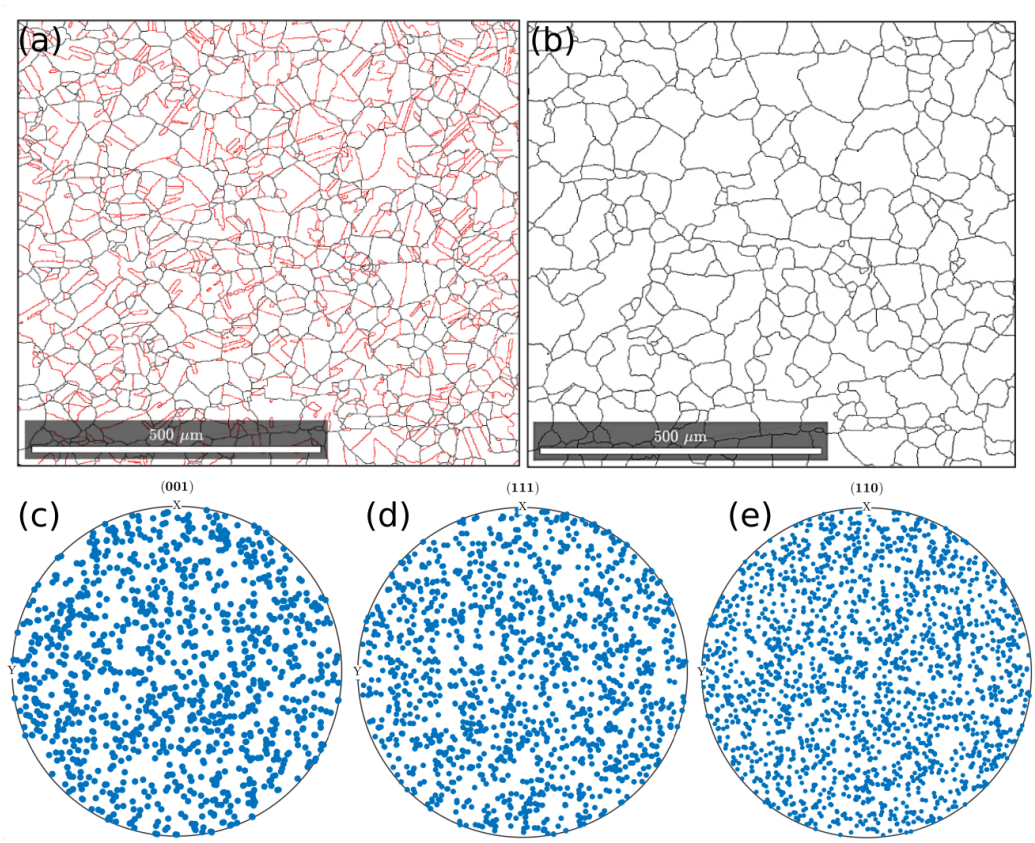

Figure 3: EBSD map of the sample before deformation with (a) and without twin boundaries (b). Twin boundaries plotted in red and grain boundaries excluding twins plotted in black. (001), (111) and (110) pole figures (c-e).

For the deformed samples figure 5 shows the evolution of the microstructure, with the increase in strain, in terms of GAM values and recrystallized grains for one set of deformation conditions. The evolution of the microstructure, from the initial state characterized by $\bar{D}_{N2D} = 43.1$ (μm) and $\bar{D}_S = 75.6$ (μm), in terms of recrystallized fraction, average grain size by number and by surface, are shown in figure 6 for the considered deformation conditions.

The results show that, the change in strain rate does not have significant effects in the evolution of the recrystallized fraction, while the increase in temperature causes an increase in the recrystallized fraction. In terms of grain size, the evolution of the grain sizes by surface shows that neither the changes in temperature or strain rates, causes a consistent change in the grain

size evolution at all the considered deformation levels. $\bar{D}_S$ for the highest strain rate, shows an unexpected behaviour with significantly higher values at $\epsilon = 1.0$, than the other strain rates, this behaviour is likely to be due self-heating. In all cases even at low recrystallized fraction levels there is a significant reduction form the initial grain sizes, this is caused in part by the twin identification issue described above.

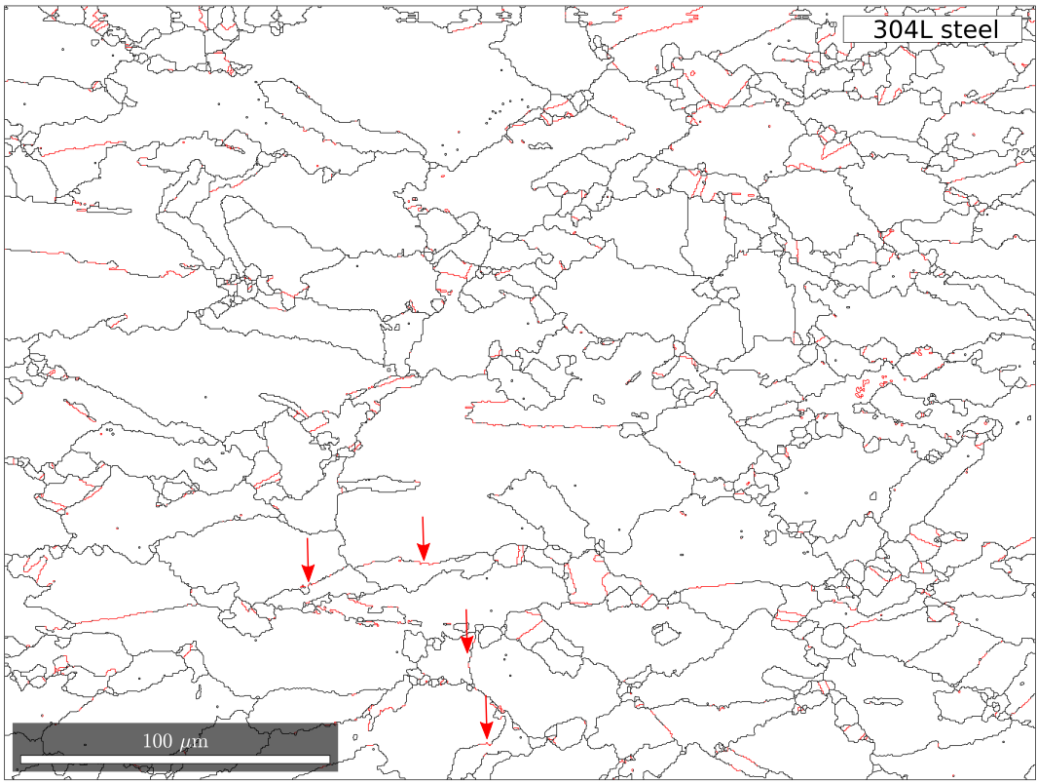

Figure 4: EBSD maps of the sample deformed at $T = 1273\ K\ -\dot{\epsilon} = 0.014\ s^{-1}\ -\epsilon = 0.65$. Twin boundaries plotted in red and grain boundaries excluding twins plotted in black.

For the 3D measurements, the evolution of the microstructure in terms of $\bar{D}_{N3D}$ and $\bar{D}_V$, from the initial state of $\bar{D}_{N3D} = 33.2\ \mu m$ and $\bar{D}_{N3D} = 86.5\ \mu m$,considering all the grains (the recrystallized grains and the non recrystallized ones), for the different deformation conditions are shown in figure 7.

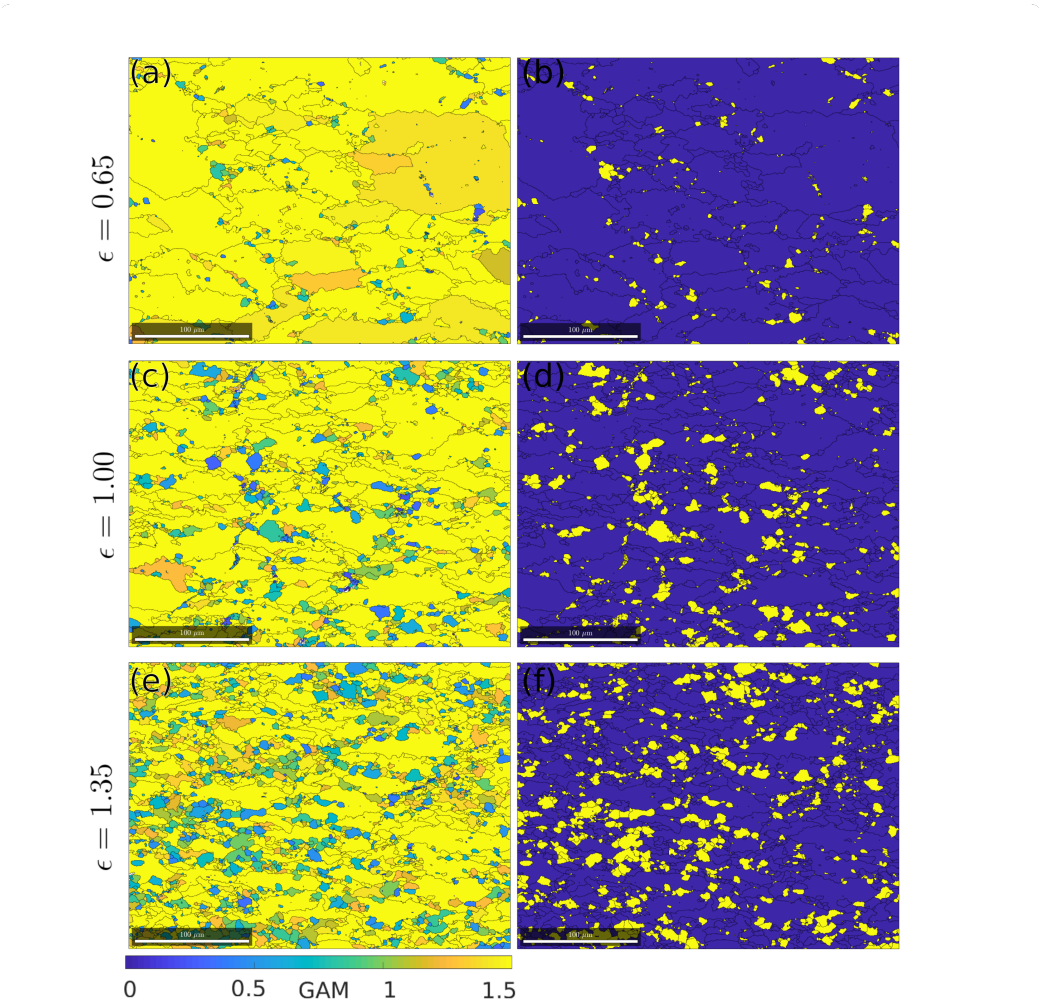

Figure 5: EBSD maps at different strain levels of the sample deformed at $T = 1000\ K\ -\ \dot{\epsilon} = 0.07\ s^{-1}$ with grain boundaries plotted in black. (a,c,e) Grains colored by GAM value. (b,d,f) Recrystallized grains (yellow) and non-recrystallized grains (blue).

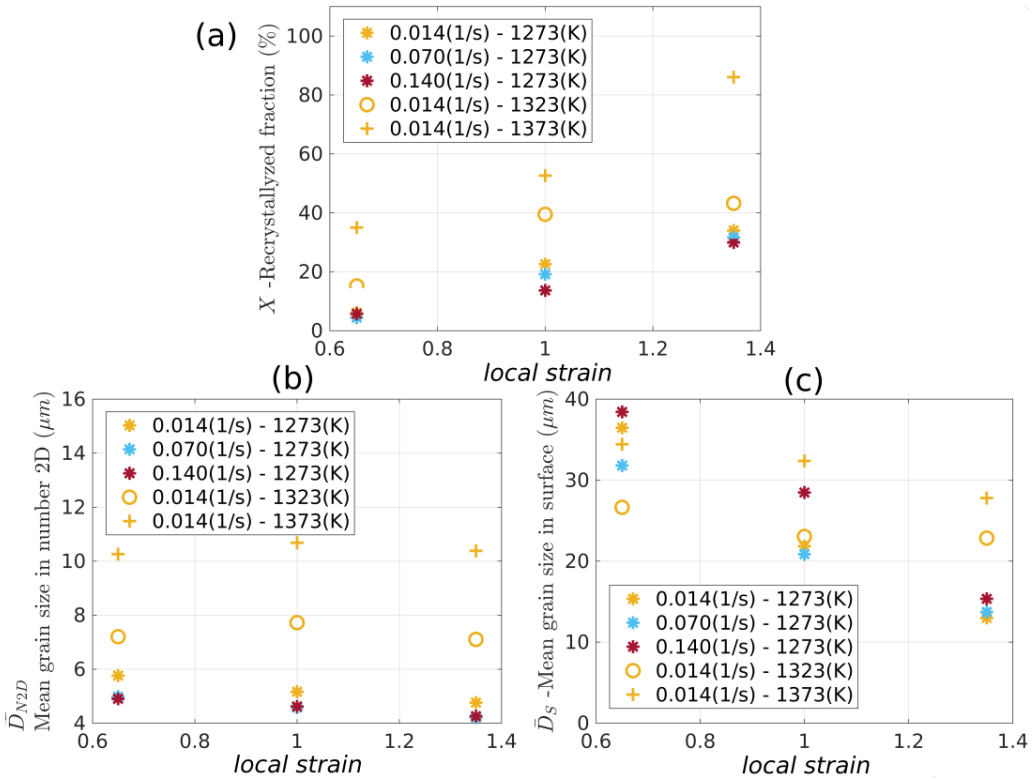

Figure 6: Evolution of X (a), $\bar{D}_{N2D}$ (b) and $\bar{D}_S$ (c) as a function of strain for the different deformation conditions.

The results show that the behaviour considering all the grains is consistent with the behaviour observed for the 2D data. With the increase in temperature the final grain size increases, and the final grain sizes for the different strain rates are very similar. For the recrystallized grains, for a given deformation condition there is no significant change in the mean size of the recrystallized grains for the different strain levels. There is a small increase in size between the lower strain level and the middle strain level, but at the higher strain level the size shows almost the same value that at the middle strain level. The increase in temperature also leads to higher mean recrystallized grain sizes, while the change in strain rate shows little influence. For the non recrystallized grains, the significant reduction in grain size between the non deformed state and the first measurement after deformation, is seen clearly.

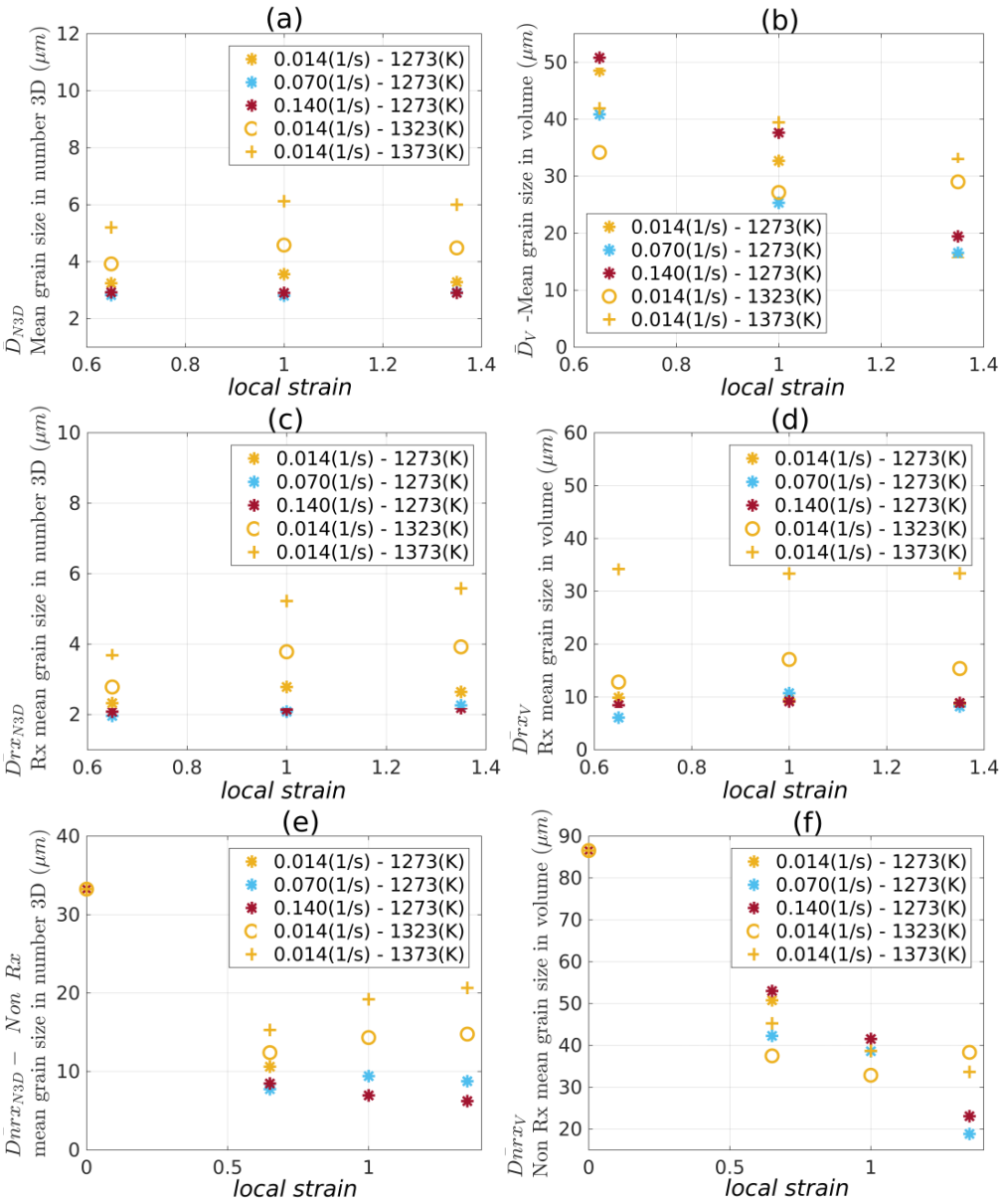

Figure 7: Evolution of $\bar{D}_{N3D}$ (a,c,e) and $\bar{D}_V$ (b,d,f) as a function of strain, considering all the grains (a,b), the recrystallized grains (c,d) and the non recrystallized grains (e,f) for the different deformation conditions.

In terms of distributions, the results for one of the considered deformation conditions are shown in figure 8. Both the distributions by surface and

volume show that the microstructure contains a significant fraction of grains with sizes much smaller and much bigger than the mean value. The distributions do not present a regular shape that can be correctly fitted with the commonly used normal or log normal mathematical distributions.

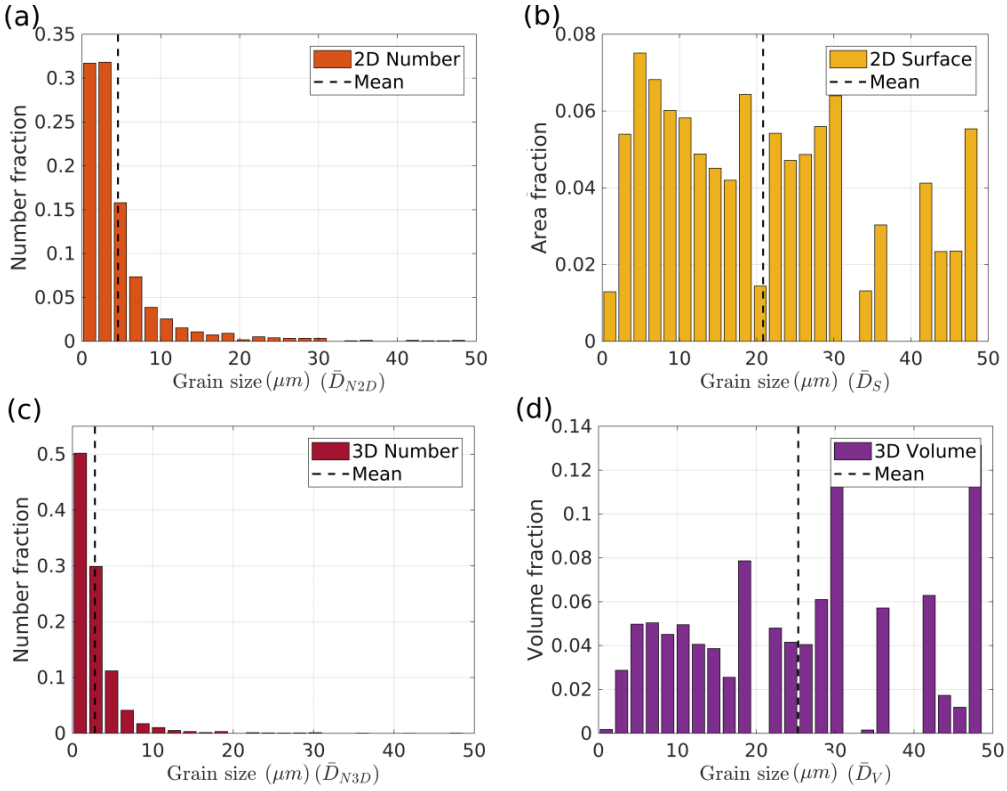

Figure 8: Grain size distributions by number fraction 2D (a), surface fraction(b), number fraction 3D (c) and volume fraction (d). Sample deformation conditions $T = 1273\ K - \dot{\epsilon} = 0.07\ s^{-1}\ - \epsilon = 1.0$.

4. Calibration and validation of the Numerical Model

4.1. Parameter identification procedure

The numerical model used in this work couples a level-set based numerical framework for microstructural evolution simulation with a crystal plasticity finite elements method (CPFEM). The model provides 3D full field simulations of dynamic recrystallization up to high strains with topological

description of grains. The details of the model can be found in [1], will not be detailed here.

The model was calibrated by performing inverse analysis, using the optimization tool Moopi [29]. The experimental data was divided into one set of data used for calibration and other set used for validation, as depicted in table 1. The process was performed in two steps. First only the crystal plasticity model parameters were calibrated and validated against the experimental stress-strain curves before DRX onset. Second with the obtained parameters for the crystal plasticity part, the coupled model parameter was calibrated and validated against the recrystallization kinetics obtained from the EBSD maps.

For the first part, the parameters $K1$ and $K2$ were calibrated, these parameters represent the generation of dislocations due to plastic deformation and their disappearance by dynamic recovery respectively, in the dislocation density (ρ) evolution law considered in the model:

$$\dot{\rho} = \left(\frac{K_1}{M} - \frac{K_2}{M}\rho\right) \sum_{\alpha=1}^{n} \mid \dot{\gamma^{\alpha}} \mid , \tag{8}$$

with M the Taylor factor and $\dot{\gamma^{\alpha}}$ the strain rate on the slip system α. The parameters $K1$ and $K2$ are also included in the calculation of the critical dislocation density ρ_{cr}, which defines the start of nucleation and the size of the inserted recrystallized grains (r^*):

$$\rho_{cr} = \left[\frac{-2\gamma_b \dot{\epsilon} \frac{K_2}{M_b {d_e}^2}}{ln\left(1 - \frac{K_2}{K_1 \rho_{cr}}\right)}\right]^{1/2} , \tag{9}$$

$$r^* = \omega \frac{2\gamma_b}{\rho_{cr} d_e} , \tag{10}$$

with d_e being the dislocation line energy, M_b the grain boundary mobility, γ_b the unit area grain boundary energy and ω a numerical safety factor. The second part of the calibration procedure was done regarding the parameter k_g, which represents the probability of recrystallized grains appearance in the nucleation rate law used:

$$dV = k_g \phi dt , \tag{11}$$

with ϕ the total area or volume (necklace or bulk) of the grains with dislocation density higher than the critical value, and dt the time step. The remaining model parameters are presented in table 2:

Symbol	Name	Value	Units	Reference
E	Young's modulus	$[119 - 125]$	GPa	[28]
v	Poisson's ratio	0.34	$[-]$	[28]
μ	shear module	$[40 - 45]$	GPa	[28]
$\dot{\gamma}_0$	Ref. slip rate	0.001	$[s^{-1}]$	[30]
m	slip rate sensibility	0.05	$[-]$	[30]
M	Taylor factor	3	$[-]$	[31]
ψ	substructure type	0.15	$[-]$	[32]
b	Burgers vector	$2.5 * 10^{-10}$	m	[33]
σ_0	yield stress	$[20 - 80]$	MPa	[28]
M_b	GB mobility	$[0.51 - 3.47] * 10^{-12}$	m^4/Js	[34]
d_e	disl. line energy	$1.47 * 10^{-9}$	J/m	[35]
γ_b	GB energy	0.6	J/m	[22]
ρ_0	min disl. density	$1 * 10^{11}$	m^{-2}	[36]

Table 2: Values of the model parameters for the considered thermo-mechanical conditions.

For the simulations the imposed boundary conditions represent a channel die compression with a constant strain rate. This type of boundary conditions, without free surfaces, are imposed to prevent the polycrystal from collapsing onto itself due to the rotation of some grains caused by the plastic deformation. For $304L$ steel, the deformation resulting from the imposed boundary conditions is an acceptable representation of the experimental compression tests. Figure 9 illustrates the imposed boundary conditions and figure 10 illustrates the general simulation framework.

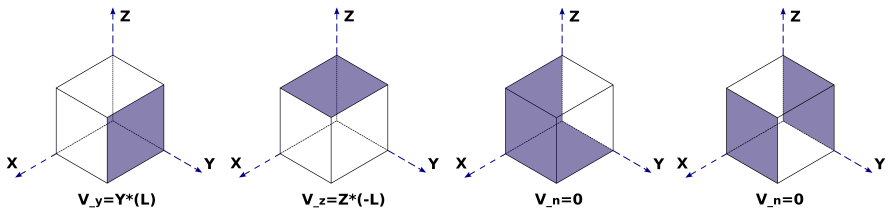

Figure 9: Boundary conditions for the simulations.

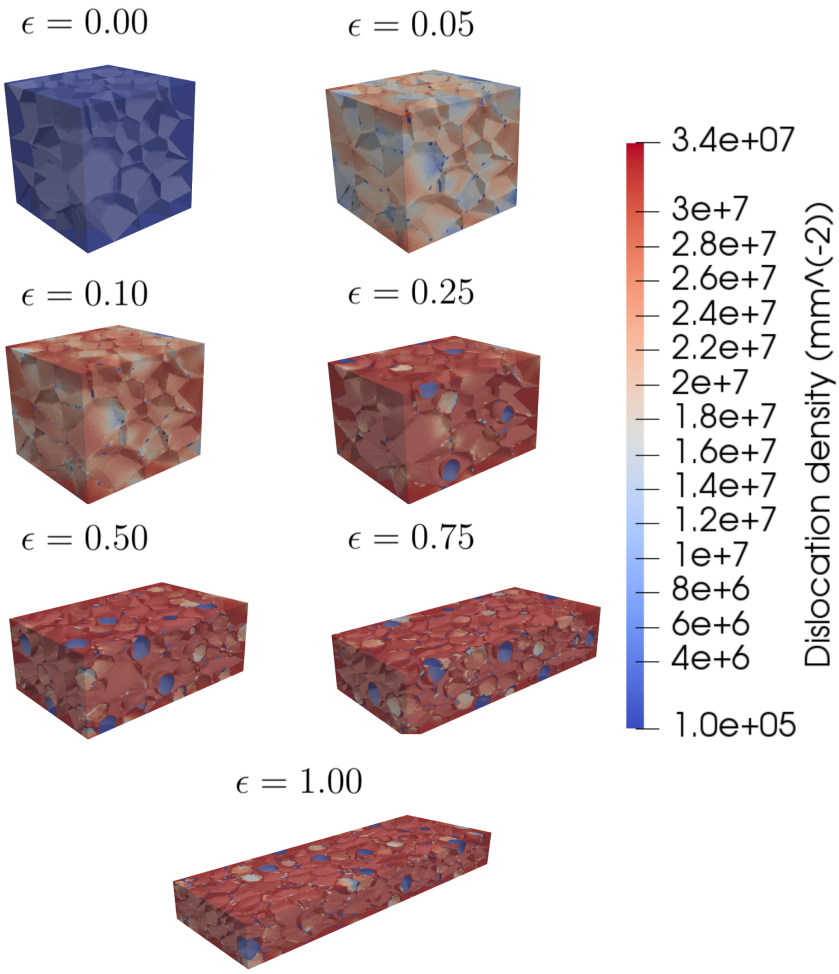

Figure 10: Example of the simulation framework.

4.2. Calibration and validation of the CPFEM model

For the calibration and validation of CPFEM model the data considered was: up to $\epsilon = 0.25$ for $T = 1273(K)$, and up to $\epsilon = 0.20$ for $T = 1323(K)$ and $T = 1373(K)$. This is done in order to minimize the effect of recrystallization in the stress response. Only the effects of strain hardening and dynamic recovery are considered, which are the two phenomena related to the parameters K_1 and K_2.

Figure 11 (a,b) shows the results of the calibration procedure. In general terms, the model results show good agreement with the experimental results.

The largest differences are seen in the initial part of the curves, specially for higher temperatures, they are related to the chosen σ_0 value.

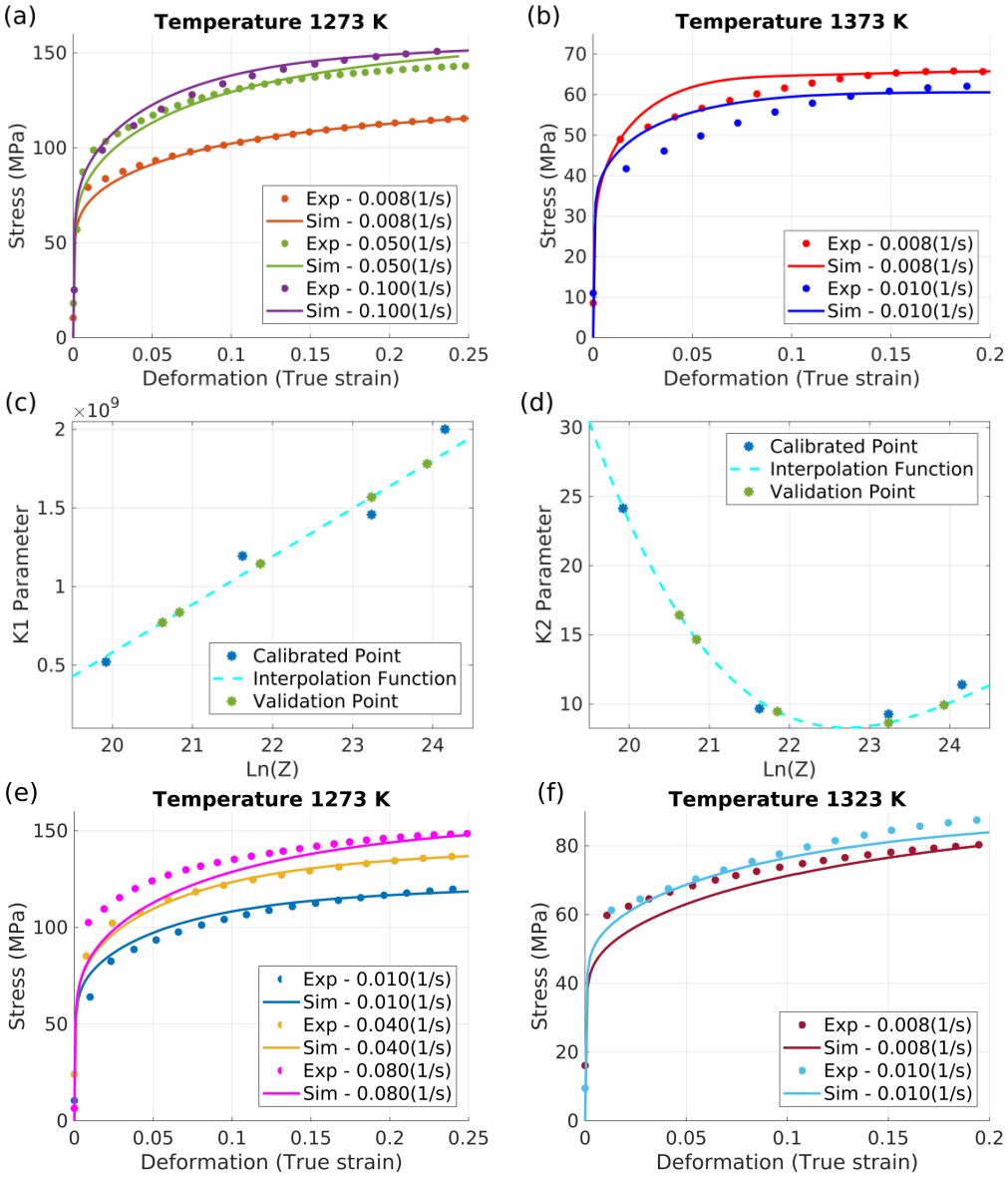

Figure 11: Comparison between the CPFEM model results and the experimental results, stress-strain curves. Calibration (a,b), Parameters evolution (c,d) and Validation(e,f).

The identified parameter values were used to construct functions that de-

scribe the evolution of model parameters as a function of the Zener Hollomon parameter ($Z = \dot{\epsilon}\ exp(Q/RT)$). The identified values and their corresponding functions are also shown in figure 11 (c,d).

With the constructed functions, the parameters value for the thermomechanical conditions set for validation of the model were calculated and simulations were run for these thermomechanical conditions. The simulated results compared to experimental measurements are presented in figure 11 (e,f). The results are consistent with the results observed in the calibration procedure, showing that the model predictions are in good agreement with the experimental measurements. The largest differences are also observed in the initial part of the curves, this can be partially explained by the uncertain in the identification of σ_0 in the experimental curves.

4.3. Calibration and validation of the coupled model

Figure 12 (a,b) shows the results of the calibration procedure for the coupled model. The results show good agreement in terms of recrystallized fraction. For the average grain size ($\bar{D}_V$) there is an important difference between the model results and the experimental data at higher strains, this will be further discussed in section 5.

The identified parameter values were used to construct a piece-wise linear function that describes the evolution of the parameter k_g in terms of the thermo-mechanical conditions described by the Z parameter. This type of function was used due to the limited number of points. The identified values and the interpolated function are shown in figure 12 (c).

Following the previously described procedure the interpolated function is used to calculate the parameter value (figure 12 (c)) for the thermomechanical conditions chosen to validate the model. The results are shown in figure 12 (e,f). The results show the same trend as the results observed in the calibration. The model correctly predicts the recrystallized fraction, but shows some errors in average grain size value predicted at higher strains.

The disagreement between the model results and the experimental data, in terms of mean grain size ($\bar{D}_V$), can be explained by several factors related mainly to the twin boundaries and the size of inserted recrystallized grains. These limitations of the proposed model and the calibration procedure are discussed in section 5.

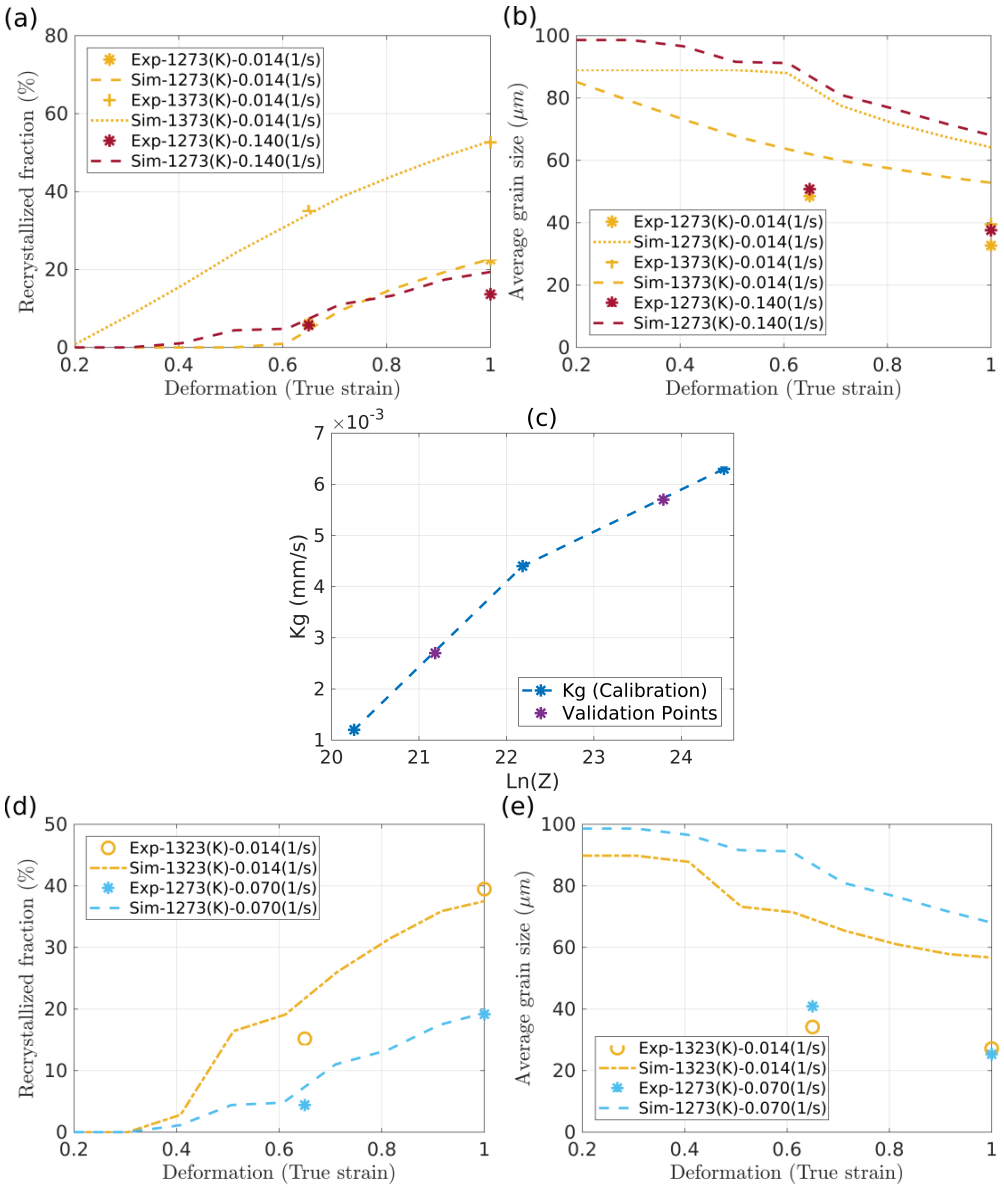

Figure 12: Comparison between the coupled model results and the experimental results, recrystallized fraction (a,d) and average grain size ($\bar{D}_V$) (b,e). Calibration (a,b), Parameters evolution (c) and Validation(d,e).

5. Model discussion

5.1. Recrystallized grains size and Twin grain boundaries

Two limitations were identified when comparing the model with experimental data. First the size of inserted recrystallized grains calculated according to eq. 10, that depends on the values of the parameters K_1 and K_2, defines a size over the measured recrystallized grains size. Figure 13 shows the modeled recrystallized grains size compared to measured experimental recrystallized grain size at $\epsilon = 0.65$ for the different thermomechanical conditions. This over prediction of the recrystallized grains size introduces errors in the model predictions.

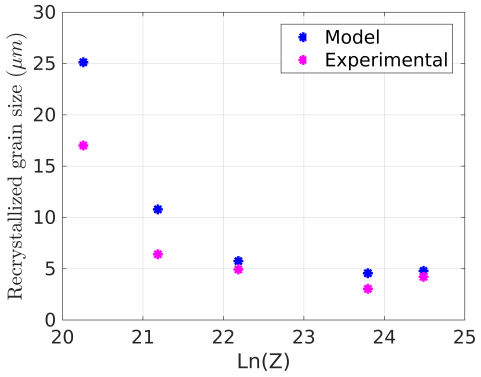

Figure 13: Model recrystallized grains (r^*) size compared with measured experimental recrystallized grain size at $\epsilon = 0.65$ for the different thermomechanical conditions.

Second, as mentioned in section 2 and illustrated in figure 4, the difficulties to identify twin boundaries on deformed microstructures, introduce an artificial reduction in the experimental grain sizes as strain increases. This effect is illustrated by the evolution of the mean grain size of the non recrystallized grains, presented in figure 7. The results show a higher reduction in the grain size between the non deformed state and the first deformed state, which can not be explained only by the effects of recrystallization at such low strain.

To circumvent these two limitations: First a re-calibration of the parameters K_1 and K_2 was performed, the objective was to define K_1 and K_2 values that give the same mechanical behaviour but define a smaller recrystallized grain size. To do this, the parameter $k_0 = \sigma_0/M$ that defines the

initial microscopic yield stress of the material, and the parameter m that represents the flow rule sensitivity in the crystal plasticity model, were also introduced into the calibration parameters. By using this procedure, for the deformation conditions $\dot{\epsilon} = 0.014(s^{-1})$ $T = 1273(K)$ the model recrystallized grain size was reduced from $r^* = 24.87\ \mu m$ with the initial parameters to $r^* = 11.45\ \mu m$ with the new parameters. This reduction in the model recrystallized grain size, involves a significant increase in the computational cost as the mesh size is defined according to the r^* value [1].

Second, to address the twin boundaries identification issue a second initial digital microstructure was generated. This microstructure follows the experimental grain size distribution but considering twin boundary as general grain boundary in the grain detection procedure. Figure 14 shows the grain size distributions for the two cases. However, the current framework does not consider heterogeneous grain boundary energy, so the effect is only related to the initial grain size. One of the perspectives of this work is then to enhance the current framework to consider heterogeneous grain boundary energy following the works of [37].

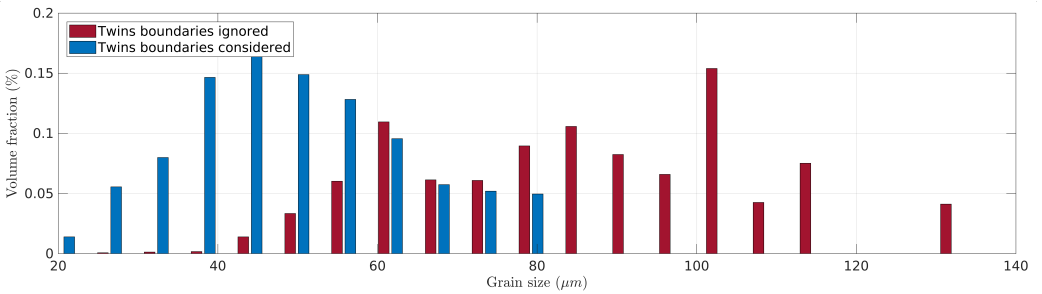

Figure 14: Grain size (d_{3D}) distributions by volume of the initial digital microstructures considering and without considering twin boundaries in the grain detection procedure.

Simulations were run with the new parameters and with the two initial microstructures, the simulation with the initial microstructure generated ignoring twin boundaries is further mentioned as case 1, and the the simulation with the initial microstructure generated considering twin boundaries as regular grain boundaries is further mentioned as case 2. The results are shown in terms of average behaviour in figure 15, and in terms of grain size distributions by volume at $\epsilon = 1.0$ deformation levels in figure 16.

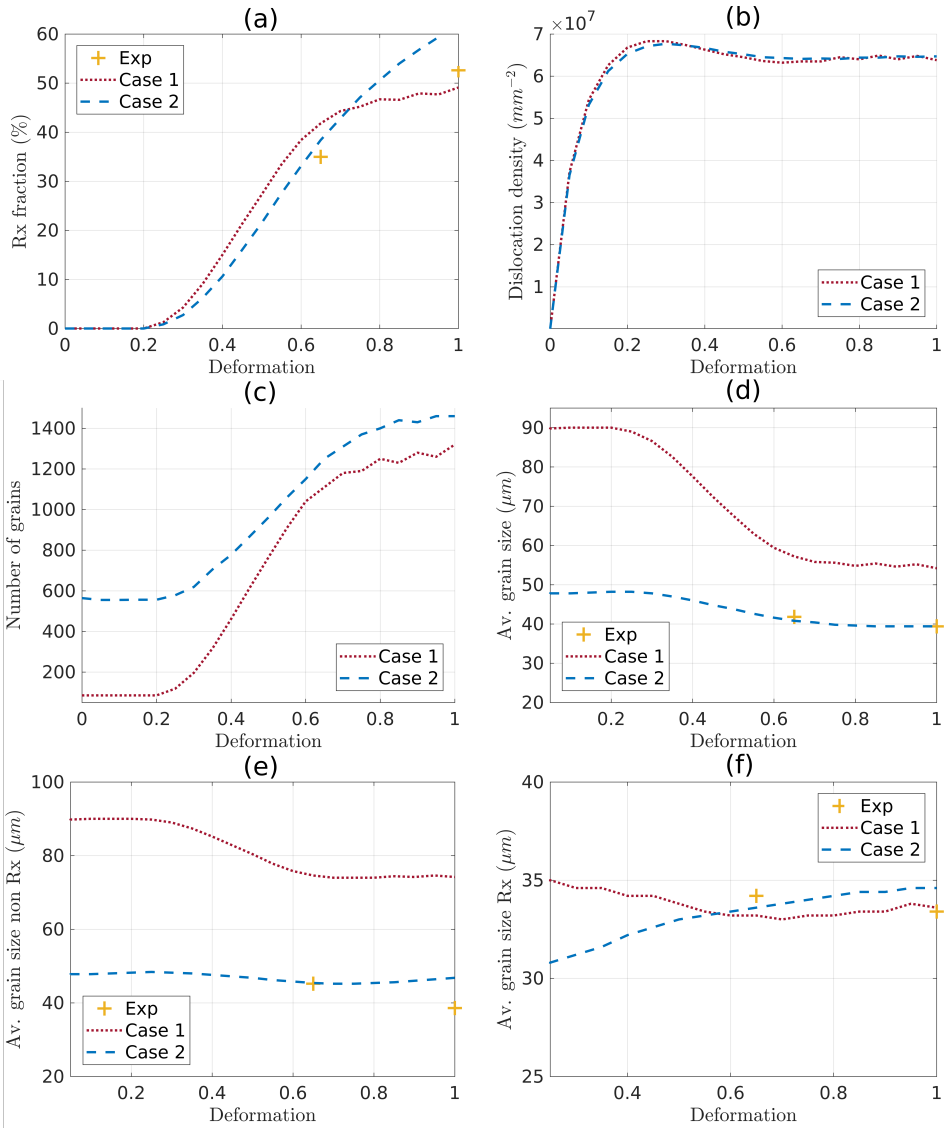

Figure 15: Comparisons of simulation results for both cases with different initial microstructure with experimental data in terms of average behaviour. (a) Recrystallized fraction, (b) dislocation density, (c) number of grains, (d) average grain size ($\bar{D}_V$), (e) average non recrystallized grain size ($\bar{D}_{NRxV}$), (f) average recrystallized grain size ($\bar{D}_{RxV}$).

The results show that by improving the parameters to define a smaller nucleus, consistent with the experimental data, the numerical predictions better fit the experimental data. The average dislocation shows a very similar

behaviour in both cases, meaning that the number of initial grains and their sizes does not have significant effect in how the average dislocation density evolves. This will be further discussed in the next section. However there are differences in the evolution of microstructure.

The evolution of the average grain size ($\bar{D}_V$) shows that: the reduction of the average grain size is dependent to the difference between the initial grain size and inserted recrystallized grains size. A bigger difference, translates in a bigger reduction in the average grain size. This is also observed for the non recrystallized grains evolution.

For both cases the model correctly reproduces the evolution of the recrystallized fraction. The simulation with the smaller initial microstructure shows a higher recrystallized fraction at high deformation levels, while the simulation with a bigger initial microstructure shows a higher recrystallized fraction at the lower deformation levels. The observed behaviour is consistent with the evolution of the average recrystallized grains size ($\bar{D}_{RxV}$), which at lower deformation levels shows higher values, but with the increase in deformation this behaviour inverses.

This difference of behaviour is caused by: First, the higher number of grains boundaries that allow recrystallized grains to appear on more places, causing less clustering between them, this effect was already discussed in [1]. Second, the smaller differences in size between the recrystallized grains and non recrystallized grains, which translates in similar capillarity effects. As, when the recrystallized grains harden, the capillarity effect become the main driving force in the GB migration.

Therefore the simulations results show that having bigger grains can favor recrystallization at lower deformation levels when the recrystallized fraction is lower. But at higher deformation levels when there is a higher number of recrystallized grains in the microstructure, having smaller grains which translates in less clustering between them and smaller differences in the capillarity effect, allows the recrystallized grains to growth more quickly.

In terms of grain size distributions (figure 16) one can summarize the results as: Case 1, shows a higher percentage of big grains, than case 2 and in experimental data, even though the sizes and the percentages of the bigger grains in the microstructure has been significantly reduced with respect to the initial state. This behaviour is a clear indicator of the limitations of not including twins in the microstructures, as these big grains are not consumed in the simulation by the effects of recrystallization.

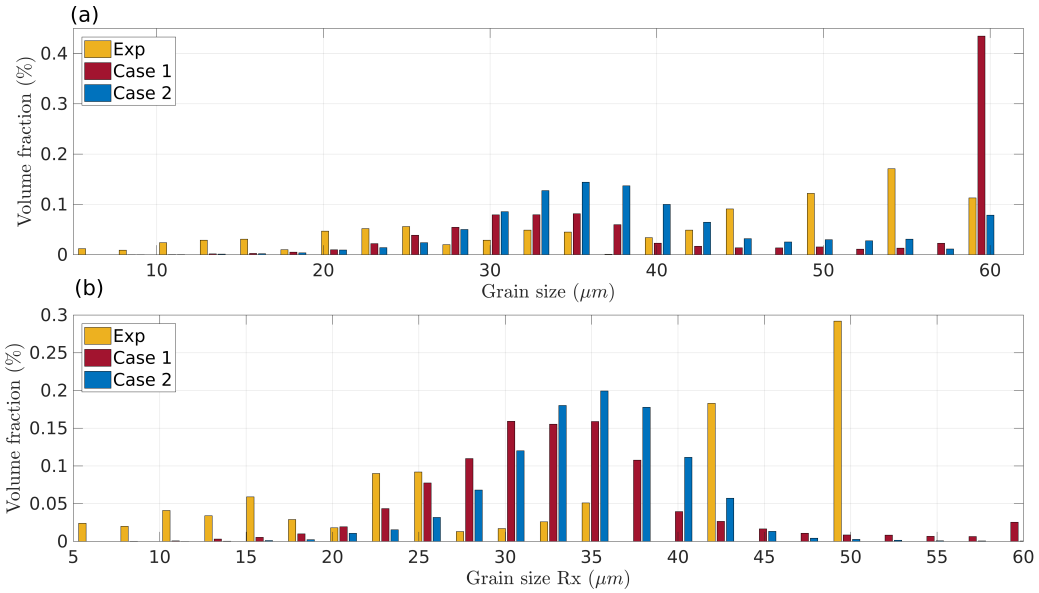

Figure 16: Comparisons of simulation results for both cases with different initial microstructure with experimental. Grain size (d_{3D}) distributions by volume. All grains (a) and recrystallized grains (b)/

Regarding the recrystallized grains distributions, which at this deformation level ($\epsilon = 1.0$) are the majority of grains in the microstructure, the results show that in both simulations cases the recrystallized grains grow less than in experimental data. From the initial insertion diameter of $2 * r^* = 22.90\ \mu m$, most of the simulation recrystallized grains grow to sizes between 30 μm and 40 μm while in the experimental data the recrystallized grain sizes reach values around 50 μm. Due to the model formulation, recrystallized grain sizes smaller than the insertion size are very difficult to capture as recrystallized grains are inserted with a size that ensures their growth.

One alternative to improve this behaviour is instead of using a constant insertion size for the recrystallized grains, use a size distribution based on experimental data. The simulation results compared with experimental data in terms of grain size distribution at $\epsilon = 1.0$ deformation level are shown in figure 17.

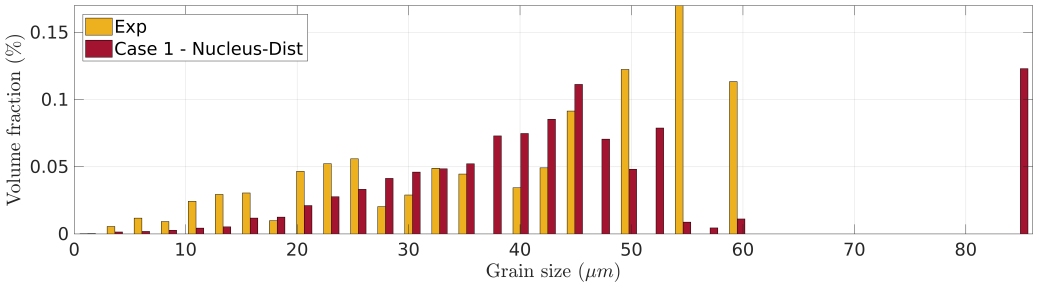

Figure 17: Comparisons of simulation results for case 1, defining r^* as a size distribution, with experimental data. Grain size (d_{3D}) distribution by volume.

The results show that with this alternative the simulation results fit more closely, the experimental data, specially for the smaller grains, however this approach is restrictive since it requires additional data to define the grain size distribution. Additionally differences in the rate of growth of the microstructure are still observed, similar to the other cases.

The results show a significant improvement with respect to the initial calibration procedure, however the model still present limitations related to grain boundary migration. Further work in the definition of the grain boundary mobility and grain boundary energy must be performed in order to improve the model capability.

5.2. Dislocation density evolution

The main advantage of including CPFEM is to obtain a better description of the evolution of the dislocation density and the orientations of the grains during DRX. However the current framework does not consider yet the grains orientation in the GB migration calculations, they only influence the deformation in the CPFEM model, so the most relevant variable is the dislocation density evolution.

In the current framework the evolution of dislocation density evolution is defined by a saturation type hardening law, the Joshie-Laasraoui-Jonas (YLJ) equation [38]. This law is a simplified model, that was used due to the limited experimental data available to identify the material parameters. It defines a maximal value for the dislocation density, thus at high deformation levels when a significant part of the microstructure has reached the saturation value, the heterogeneity in the microstructure is significantly reduced as illustrated in figure 10. The exceptions are recrystallized grains as they

are inserted with a minimal dislocation density and zones swept during GB migration. Since these zones are also subjected to deformation, they also harden and later reach the saturation value.

However, considering that the energy gradient is the dominant force in GB migration during DDRX, even if the percentage of these grains is low their effect is significant in the microstructure. So, to better describe the dislocation density evolution, distributions by volume fraction are presented in figure 18, for one simulation case.

Figures 10 and 18 show that: At low deformation levels, before nucleation has started $\epsilon < 0.20$, there is significant heterogeneity in the distribution of the dislocation density in the microstructure. The effect of the grain orientation is clear with zones in the microstructure showing low and high dislocation density levels.

At higher deformation levels most of the grains present in the microstructure ($\approx 80\%$) have a dislocation density equal to the maximal value. On these grains that have already reached the maximal dislocation density value, only zones near boundaries that have been swept due to grain boundary migration show different dislocation density levels (figure 10).

Considering only the case of recrystallized grains, the results show that condition is similar with the majority of the grains ($\approx 75\%$) having the maximal dislocation density. These are the recrystallized grains, that have already hardened and can also serve as nucleation sites.

However the remaining recrystallized grains show dislocation density levels among a wide spectrum. Figure 18 (d) shows dislocation density distribution considering only recrystallized grains with dislocation density lower than the maximal value. These results show that of these remaining grains only ($\approx 5\%$) show the minimal dislocation value, these are the grains that just appeared in the microstructure and have not deformed yet. The other recrystallized grains show several dislocation levels which is the effect of the different hardening rates caused by the differences in orientations.

These results illustrate the effect of including CPFEM in the model, they also show two future perspectives: First, for the current framework (considers homogeneous grain boundary energy) replace CPFEM with a simplified Taylor models could provide similar results with a reduction in the computational cost. Second, since the currently used hardening law is an important simplification of the dislocation density evolution, it is necessary to evaluate more complex laws that provide a better description of the evolution of the dislocation density.

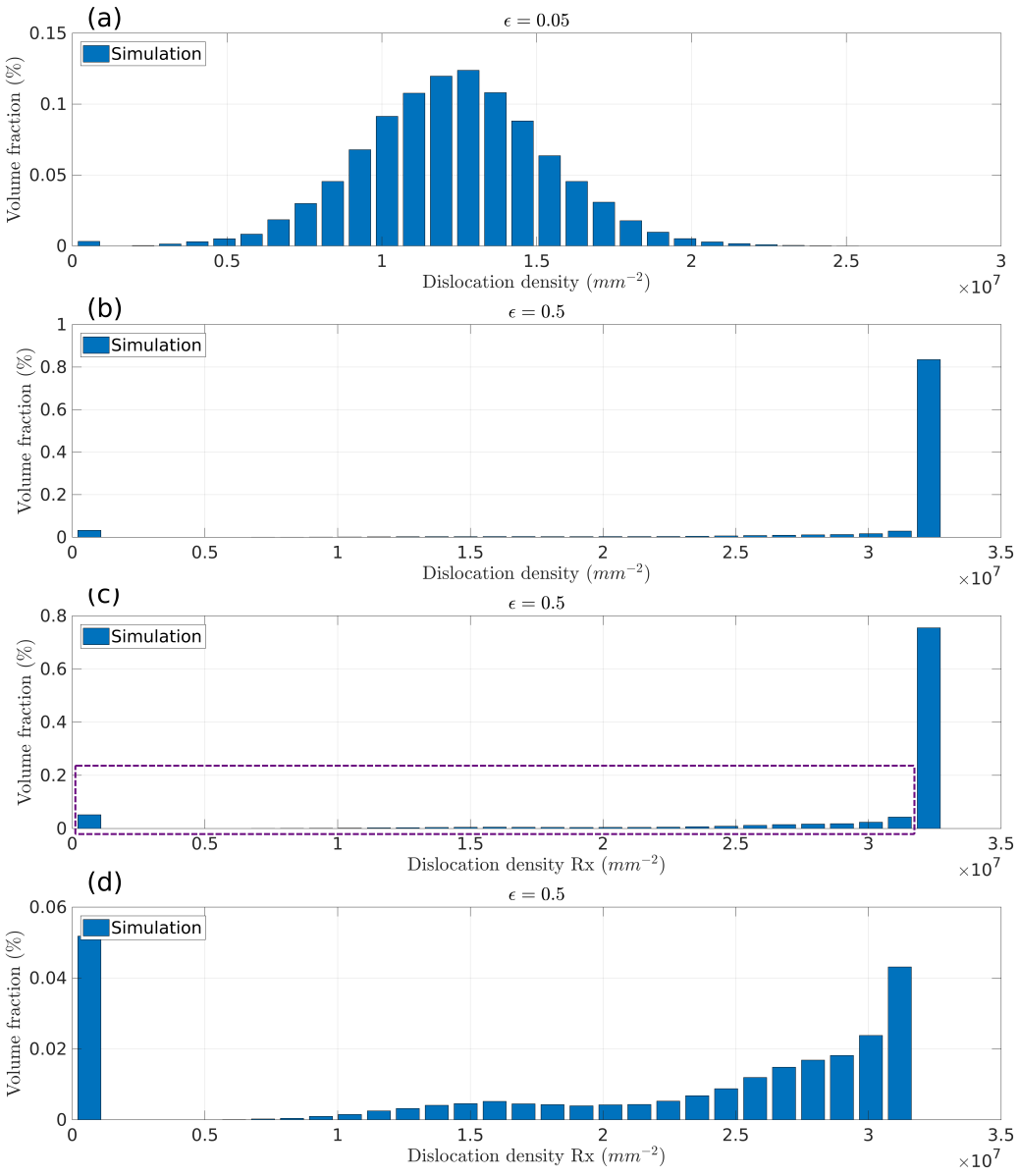

Figure 18: Evolution of the dislocation density in terms of volume distribution during DRX simulation. (a) All grains $\epsilon = 0.05$, (b) All grains $\epsilon = 0.50$, (c) Recrystallized grains at $\epsilon = 0.50$,(d) Zoom to recrystallized grains at $\epsilon = 0.50$.

6. Conclusions

In the present work the CPFEM model coupled with a LS-FE for grain boundary migration and phenomenological laws, to perform 3D full field simulations of DRX up to high deformation, was calibrated and validated with experimental measurements of 304L steel subjected to hot deformation.

The model parameters K_1, K_2 and K_g, related to the strain hardening, dynamic recovery, and nucleation probability were identified, for a range of strain rates between $0.008 - 0.1$ $(1/s)$ and temperatures between $1273 - 1373$ K. Results showed that, the calibration of the parameters K_1, K_2 considering only the stress-strain behaviour can lead to the definition of nucleus sizes that do not agree with the experimental data. Additional calibration steps, that considered also the grain size evolution must be included in order minimize these errors.

For the considered deformation conditions, the model correctly predicts the general behavior of several of the main variables of interest during dynamic recrystallization. However the grain size distribution showed that the rate of growth of recrystallized grains is still not correctly modeled. Additionally not being able to model the behaviour of twin grains boundary presents an important limitation.

Comparisons considering different initial grain sizes showed that, smaller grain sizes in the initial microstructures favors recrystallized grains growth. As having smaller grains translates into higher number of grain boundaries that serve as nucleation sites, so recrystallized grains can be appear further form each other. This reduces clustering between the recrystallized grains which can limit their growth. Also, when recrystallized grains harden, since the main driving force in their growth is the capillarity effect, having a similar size than non recrystallized grains increases the probability that they will not be consumed.

Additionally the CPFEM calculations showed that, during most of the DRX process the dislocation density of the microstructure is not that heterogeneous, as most of the grains reach the maximal dislocation density value. The grains that are constantly evolving are only the recrystallized grains, from the time that they are introduced until they completely hardened. This time window depends on the hardening rate, which can change according to the grain orientation and location.

The lack of heterogeneity also indicates that similar results could be obtained with a simplified Taylor model, reducing the computational cost. How-

ever this behaviour is also the result of chosen hardening law, which is an important simplification of the dislocation density evolution, and considering homogeneous grain boundary energy. This will be tested in future work.

In summary the coupled model constitutes a good first approach to improve dynamic recrystallization modeling. However it is still necessary to further study aspects like, effect of hardening laws, texture prediction, grain boundary energy anisotropy, mobility anisotropy, and nucleation models. Furthermore it is necessary to enrich the available database and perform similar analysis with other materials.

7. Appendix - Recrystallized grains identification

Comparing simulation data with experimental data for recrystallization processes is limited by the difficulty in identifying recrystallized grains on experimental samples, specially for full field models that aim to provide a spatial reproduction of the microstructure evolution. On simulation models the recrystallized grains can be clearly tracked and identified, since they appear. However, this is not possible on experimental samples. The procedure used in this work to identify recrystallized grains uses the GAM criteria, following the work of [26], is a procedure commonly used in the literature.

This procedure relies on establishing a GAM threshold, also the calculation of the GAM value depends on the KAM value, whose calculation depends on the spatial resolution of the measurement and the order of neighbours considered. Figure 19 shows the changes in the recrystallization fraction value, for the sample deformed at $\dot{\epsilon} = 0.014\ s^{-1}$ $T = 1323\ K$ and $\epsilon = 1.0$, for different GAM thresholds and different order of neighbours, considered in the identification of recrystallized grains. These results show the degree of variation derived from the difficulties in the identification of recrystallized grains on experimental samples.

These difficulties translates directly to the calibration and validation of simulation models, and need to be considered, this is specially significant in this work since it was shown that the evolution of the microstructure in terms of grain size, depends greatly on the number of recrystallized grains introduced and their size. The number of grains introduced is defined in order to fit the recrystallized fraction. So, introducing a simulation criteria that is more close to the one used in experimental samples, could lead to a better modeling of the microstructure evolution, and needs to be further evaluated.

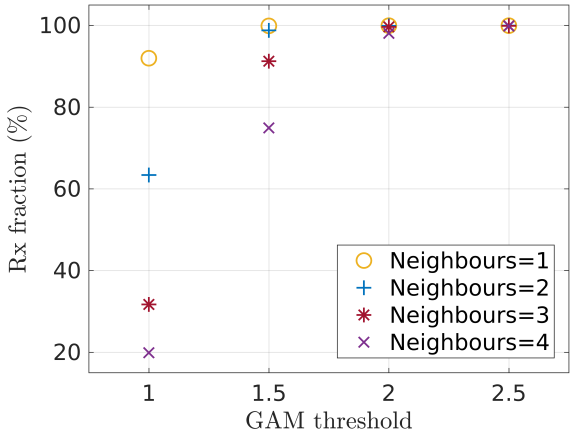

Figure 19: Changes in the recrystallization fraction, for the sample deformed at $\dot{\epsilon} = 0.014\ s^{-1}$ $T = 1323(K)$ $\epsilon = 1.0$, for different GAM thresholds and different order of neighbours considered for the calculation of the KAM value, used in the identification of recrystallized grains.

Data availability

The raw data required to reproduce these findings cannot be shared at this time as the data also forms part of an ongoing study. The processed data required to reproduce these findings cannot be shared at this time as the data also forms part of an ongoing study.

CRediT author statement

- D. A. Ruiz Sarrazola: Conceptualization, Methodology, Software, Formal analysis, Data curation, Writing - original draft.
- L. Maire: Software, Investigation.
- C. Moussa: Investigation.
- N. Bozzolo: Conceptualization, Validation, Investigation, Writing - review & editing.
- D. Pino Muñoz: Conceptualization, Software, Validation, Writing - review & editing, Visualization, Supervision.

- M. Bernacki: Conceptualization, Software, Validation, Writing - review & editing, Visualization, Supervision, Project administration.

Declaration of interest

The authors declare that they have no known competing financial interests or personal relationships that could have appeared to influence the work reported in this paper.

Acknowledgments

The authors thank the ArcelorMittal, ASCOMETAL, AUBERT & DUVAL, CEA, FRAMATOME, SAFRAN, TIMET, Constellium and TRANSVALOR companies and the ANR for their financial support through the DIGIMU consortium and ANR industrial Chair. (Grant. No. ANR-16-CHIN-0001)

References

[1] D. A. Ruiz Sarrazola, D. Pino Muñoz, M. Bernacki, A new numerical framework for the full fi eld modeling of dynamic recrystallization in a CPFEM context, Computational Materials Science 179 (2020) 109645. doi:10.1016/j.commatsci.2020.109645.

[2] T. O. Saetre, O. Hunderi, E. Nes, Computer simulation of primary recrystallisation microstructures: The effects of nucleation and growth kinetics, Acta Metall. 34 (1986) 981–987. doi:10.1016/0001-6160(86)90207-5.

[3] K. Marthinsen, O. Lohne, E. Nes, The development of recrystallization microstructures studied experimentally and by computer simulation, Acta Metall. 37 (1989) 135–145. doi:10.1016/0001-6160(89)90273-3.

[4] T. Furu, K. Marthinsen, E. Nes, Modelling recrystallisation, Mater. Sci. Technol. 6 (1990) 1093–1102. doi:10.1179/mst.1990.6.11.1093.

[5] O. Beltran, K. Huang, R. Logé, R. Loge, A mean field model of dynamic and post-dynamic recrystallization predicting kinetics, grain size and flow stress, Comput. Mater. Sci. 102 (2015) 293–303. doi:10.1016/J.COMMATSCI.2015.02.043.

[6] P. Bernard, S. Bag, K. Huang, R. Loge, A two-site mean field model of discontinuous dynamic recrystallization, Mater. Sci. Eng. A 528 (2011) 7357–7367. doi:10.1016/J.MSEA.2011.06.023.

[7] L. Maire, J. Fausty, M. Bernacki, N. Bozzolo, P. De Micheli, C. Moussa, A new topological approach for the mean field modeling of dynamic recrystallization, Materials and Design 146 (2018) 194–207. doi:10.1016/j.matdes.2018.03.011.

[8] F. Montheillet, O. Lurdos, G. Damamme, A grain scale approach for modeling steady-state discontinuous dynamic recrystallization, Acta Mater. 57 (2009) 1602–1612. doi:10.1016/j.actamat.2008.11.044.

[9] M. Zouari, N. Bozzolo, R. E. Loge, Mean field modelling of dynamic and post-dynamic recrystallization during hot deformation of Inconel 718 in the absence of δ phase particles, Mater. Sci. Eng. A 655 (2016) 408–424. doi:10.1016/j.msea.2015.12.102.

[10] D. Raabe, Introduction of a scalable three-dimensional cellular automaton with a probabilistic switching rule for the discrete mesoscale simulation of recrystallization phenomena, Philos. Mag. A Phys. Condens. Matter, Struct. Defects Mech. Prop. 79 (1999) 2339–2358. doi:10.1080/01418619908214288.

[11] A. D. Rollett, D. J. Srolovitz, M. P. Anderson, Simulation and theory of abnormal grain growth-anisotropic grain boundary energies and mobilities, Acta Metall. 37 (1989) 1227–1240. doi:10.1016/0001-6160(89)90117-X.

[12] A. D. Rollett, D. Raabe, A hybrid model for mesoscopic simulation of recrystallization, Comput. Mater. Sci. 21 (2001) 69–78. doi:10.1016/S0927-0256(00)00216-0.

[13] L. A. Barrales Mora, G. Gottstein, L. S. Shvindlerman, Three-dimensional grain growth: Analytical approaches and computer simulations, Acta Mater. 56 (2008) 5915–5926. doi:10.1016/j.actamat.2008.08.006.

[14] J. Lépinoux, D. Weygand, M. Verdier, Modélisation de la croissance de grains par dynamique de vertex, Comptes Rendus Phys. 11 (2010) 265–273. doi:10.1016/j.crhy.2010.07.015.

[15] M. Bernacki, Y. Chastel, T. Coupez, R. Logé, Level set framework for the numerical modelling of primary recrystallization

in polycrystalline materials, Scr. Mater. 58 (2008) 1129–1132. doi:10.1016/J.SCRIPTAMAT.2008.02.016.

[16] M. Bernacki, R. E. Logé, T. Coupez, Level set framework for the finite-element modelling of recrystallization and grain growth in polycrystalline materials, Scr. Mater. 64 (2011) 525–528. doi:10.1016/J.SCRIPTAMAT.2010.11.032.

[17] M. Elsey, S. Esedoglu, P. Smereka, Diffusion generated motion for grain growth in two and three dimensions, J. Comput. Phys. 228 (2009) 8015–8033. doi:10.1016/j.jcp.2009.07.020.

[18] H. Hallberg, A modified level set approach to 2D modeling of dynamic recrystallization, Model. Simul. Mater. Sci. Eng. 21 (2013). doi:10.1088/0965-0393/21/8/085012.

[19] L. Maire, B. Scholtes, C. Moussa, N. Bozzolo, D. P. Muñoz, A. Settefrati, M. Bernacki, Modeling of dynamic and post-dynamic recrystallization by coupling a full field approach to phenomenological laws, Mater. Des. 133 (2017) 498–519. doi:10.1016/j.matdes.2017.08.015.

[20] C. Krill III, L.-Q. Chen, Computer simulation of 3D grain growth using a phase field model, Acta Mater. 50 (2002) 3059–3075. doi:10.1016/s1359-6454(02)00084-8.

[21] I. Steinbach, O. Shchyglo, Phase-field modelling of microstructure evolution in solids: Perspectives and challenges, Curr. Opin. Solid State Mater. Sci. 15 (2011) 87–92. doi:10.1016/j.cossms.2011.01.001.

[22] K. Huang, R. E. Logé, A review of dynamic recrystallization phenomena in metallic materials, Mater. Des. 111 (2016) 548–574. doi:10.1016/j.matdes.2016.09.012.

[23] L. Madej, M. Sitko, M. Pietrzyk, Perceptive comparison of mean and full field dynamic recrystallization models, Arch. Civ. Mech. Eng. 16 (2016) 569–589. doi:10.1016/j.acme.2016.03.010.

[24] A. D. Rollett, G. S. Rohrer, F. J. Humphreys, Recrystallization and related annealing phenomena., 3rd ed., Elsevier, 2017.

[25] F. Bachmann, R. Hielscher, H. Schaeben, Grain detection from 2d and 3d EBSD data-Specification of the MTEX algorithm, Ultramicroscopy 111 (2011) 1720–1733. doi:10.1016/j.ultramic.2011.08.002.

[26] A. Nicolay, J. M. Franchet, J. Cormier, H. Mansour, M. de Graef, A. Seret, N. Bozzolo, Discrimination of dynamically and post-dynamically recrystallized grains based on EBSD data: application to Inconel 718, J. Microsc. 273 (2019) 135–147. doi:10.1111/jmi.12769.

[27] E. Underwood, Quantitative Stereology, 2nd ed., Addison-Wesley Publishing Company, 1970.

[28] L. Gavard, Recristallisation dynamique de aciers inoxydables austenitiques de haute purete, Ph.D. thesis, Ecole Nationale Superieure des Mines de Saint Etienne, 2001.

[29] E. Roux, Assemblage mecanique : strategies de optimisation des procedes et de identification des comportements mecaniques des materiaux, Ph.D. thesis, MINES ParisTech, 2011.

[30] A. L. Fabiano, Modelling of crystal plasticity and grain boundary migration of 304L steel at the mesoscopic scale, Ph.D. thesis, MINES ParisTech, 2013.

[31] E. V. Kozlov, N. A. Koneva, Internal fields and other contributions to flow stress, Mater. Sci. Eng. A 234-236 (1997) 982–985.

[32] L. Bäcke, Modeling the Microstructural Evolution during Hot Deformation of Microalloyed Steels, Ph.D. thesis, Royal Institute of Technology Sweden, 2009.

[33] N. Yazdipour, C. H. Davies, P. D. Hodgson, Microstructural modeling of dynamic recrystallization using irregular cellular automata, Comput. Mater. Sci. 44 (2008) 566–576. URL: http://dx.doi.org/10.1016/j.commatsci.2008.04.027. doi:10.1016/j.commatsci.2008.04.027.

[34] M. El Wahabi, J. M. Cabrera, J. M. Prado, Hot working of two AISI 304 steels: A comparative study, Mater. Sci. Eng. A 343 (2003) 116–125. doi:10.1016/S0921-5093(02)00357-X.

[35] L. Maire, Full field and mean field modeling of dynamic and post-dynamic recrystallization in 3D. Application to 304L steel, Ph.D. thesis, MINES ParisTech, 2018.

[36] K. Huang, R. E. Logé, Microstructure and flow stress evolution during hot deformation of 304L austenitic stainless steel in variable thermomechanical conditions, Materials Science and Engineering A 711 (2018) 600–610. doi:10.1016/j.msea.2017.11.042.

[37] J. Fausty, N. Bozzolo, D. Pino Muñoz, M. Bernacki, A novel level-set finite element formulation for grain growth with heterogeneous grain boundary energies, Materials and Design 160 (2018) 578–590. doi:10.1016/j.matdes.2018.09.050.

[38] A. Yoshie, H. Morikawa, Y. Onoe, K. Itoh, Formulation of static recrystallization of austenite in hot rolling process of steel plate., Trans. Iron Steel Inst. Japan 27 (1987) 425–431. doi:10.2355/isijinternational1966.27.425.

Graphical Abstract

Full field modeling of Dynamic Recrystallization in a CPFEM context - Application to 304L steel

D. A. Ruiz Sarrazola, L. Maire, C. Moussa, N. Bozzolo, D. Pino Muñoz, M. Bernacki

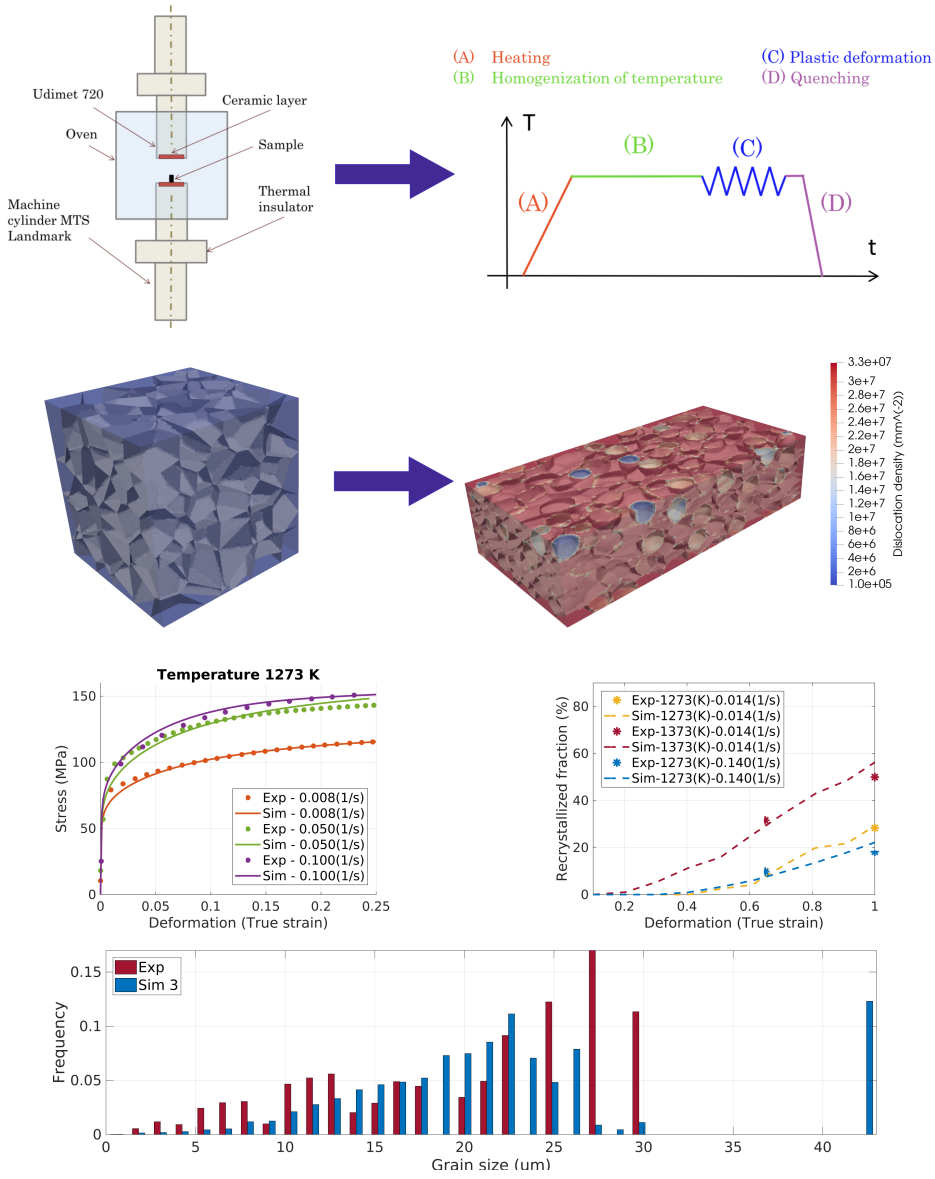

Highlights

Full field modeling of Dynamic Recrystallization in a CPFEM context - Application to 304L steel

D. A. Ruiz Sarrazola, L. Maire, C. Moussa, N. Bozzolo, D. Pino Muñoz, M. Bernacki

- 3D full field simulations of dynamic recrystallization applied to model the behaviour of 304L steel.
- Simulation results are compared with experimental stress-strain curves and EBSD measurements, for several strain rates and temperatures.
- New strategies to improve classical dynamic recrystallization models are presented and their effect on simulation results are compared to experimental measurements.